

**Title:** Low-Power Laser Micro-Shaping of Dye-Volatile Cocrystals: The Gentle Cutting Edge of Photoresponsive Materials.

**Authors:** *T. H. Borchers, F. Topić, J.-C. Christopherson, O. S. Bushuyev, J. Vainauskas, H. M. Titi, T. Friščić,\* and C. J. Barrett\**

**Address:** Department of Chemistry, McGill University, Montreal, QC, Canada

## **Abstract**

Cocrystallization of a fluorinated azobenzene with volatile cocrystal components dioxane or pyrazine yields halogen-bonded cocrystals that can be cut, carved, etched or engraved with low-powered visible laser light. This process, termed cocrystal laser micro-shaping (CLMS), is enabled by cocrystallization of a visible light dye with a volatile component, giving rise to materials that can be selectively disassembled with micrometer precision using gentle, non-burning irradiation in a commercial confocal microscope setup. The ability to shape and even machine cocrystals in 3D using laser powers between 0.5 and 20 mW, which are 2–4 orders of magnitude lower compared to laser powers used for machining metals, ceramics or polymers, is rationalized by CLMS targeting the disruption of weak supramolecular interactions between cocrystal components, rather than the breaking of covalent bonds in polymers or disruption of ionic structures required for conventional laser beam or focused ion beam machining processes, mainly by high-power laser heating.

## **Main text**

The formation of multi-component crystals (cocrystals) by the assembly of molecular building blocks with complementary molecular recognition functionalities is a well-developed strategy for

improving solid-state physicochemical properties of molecular solids,<sup>1–3</sup> such as pharmaceuticals,<sup>4</sup> photo- or thermo-responsive materials,<sup>5–7</sup> as well as for tuning the optical,<sup>8,9</sup> and conducting properties of organic materials.<sup>10</sup> Halogen bonding<sup>11,12</sup> has been used as a design element to generate dynamic cocrystals<sup>13</sup> with potential applications in stabilization or separation<sup>14</sup> of volatile molecules, as a tool for constructing amphidynamic<sup>15,16</sup> and liquid crystals,<sup>17</sup> for templating solid-state reactions,<sup>18</sup> and other uses in materials chemistry.<sup>19,20</sup>

Stimuli-responsive behaviour of molecular crystals has recently attracted great interest,<sup>21</sup> and in particular a wide range of light-matter interactions have been achieved, including chemical reactions (*e.g.* isomerization,<sup>22,23</sup> dimerization,<sup>24,25</sup> or polymerization<sup>26,27</sup>); photomechanical motion,<sup>21,28–30</sup> photochromism,<sup>31</sup> and waveguide behaviour.<sup>32,33</sup> While traditional photolithography has been applied to polymeric resins,<sup>34</sup> hyperbolic metamaterials,<sup>35</sup> nanostructures,<sup>36</sup> photonic crystals<sup>37</sup> and cocrystal thin films,<sup>38</sup> the ability to accurately shape, or machine, organic crystalline solids using low-powered visible or ultraviolet (UV) light has yet to be achieved. While machining of patterns has been reported using high-energy beam techniques, such as focused ion beam (FIB) milling,<sup>39</sup> electron beam lithography, or femtosecond laser beam machining,<sup>40</sup> these methods operate at high energies (1–50 keV) and beam powers (on the order of several Watts) that produce chemical damage to organic materials, and are most commonly used for organic polymers and inorganic materials.<sup>41–44</sup>

Here we describe cocrystallization through halogen bonding as a route to obtain crystalline organic materials that can be engraved, cut, and/or punctured without chemical damage, with micrometer-scale precision, using a laser beam with output powers in the milliwatt range (0.5–20 mW), *i.e.* orders of magnitude lower in comparison to conventional beam machining techniques, and less than that of sunlight. The herein reported cocrystals are based on a photo-responsive

building block (*trans*-4,4'-diiodooctafluoroazobenzene, *trans*-**azo**, Fig. 1a) combined with dioxane or pyrazine (Fig. 1a) as a loosely bound halogen bond acceptor, and their susceptibility to machining using a low-energy laser beam represents a new property emergent from cocrystal formation. To the best of our knowledge, this work is the first demonstration of gentle photo-machining of a molecular crystal with micrometer precision, and introduces this cocrystal laser micro-shaping (CLMS) technique, analogous to LBM yet using energies far below the threshold of chemical damage, as a methodology to shape organic crystals.

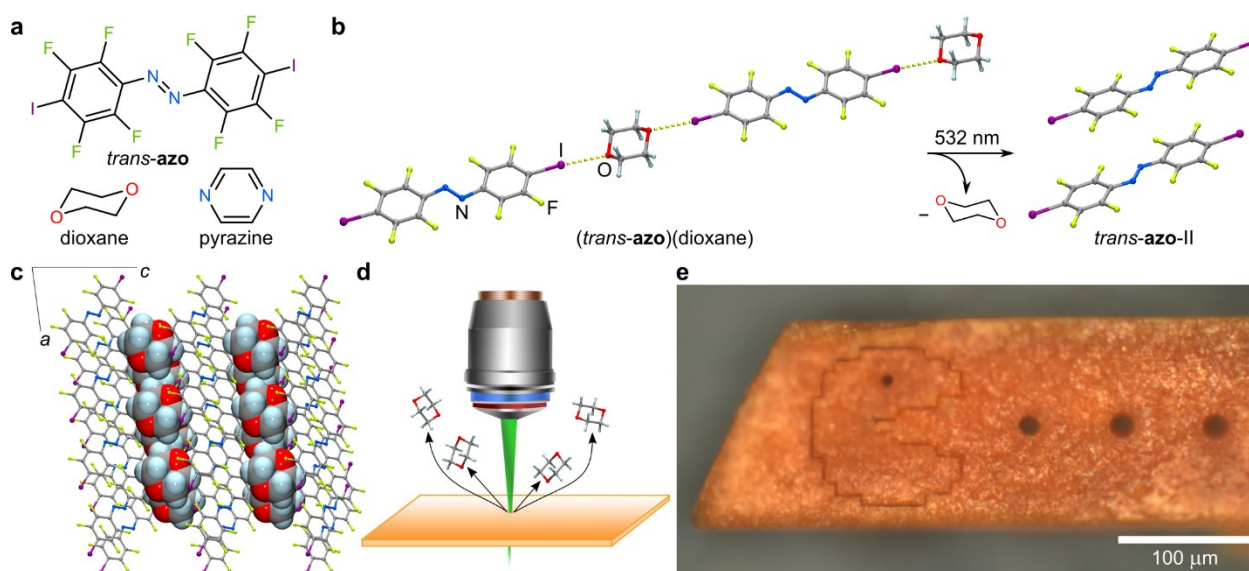


**Fig. 1 Laser beam machining of a halogen-bonded cocrystal.** **a**, Molecular structures of *trans*-**azo**, (1,4)-dioxane, and pyrazine. **b**, Illustration of the herein observed cocrystal dissociation process underlying CLMS of (*trans*-**azo**)(dioxane). **c**, Fragment of the crystal structure of (*trans*-**azo**)(dioxane), viewed along the crystallographic [010] direction. **d**, Illustration of the CLMS and/or engraving of (*trans*-**azo**)(dioxane) cocrystal using a confocal microscope system. **e**, Example of detailed CLMS of a (*trans*-**azo**)(dioxane) crystal using low-powered 532 nm light, illustrating the creation of holes, as well as surface engraving.

## Results and Discussion

### Cocrystal laser micro-shaping of (*trans*-azo)(dioxane)

The cocrystal (*trans*-azo)(dioxane) was synthesized as a part of our larger research program towards controlling the optical and photomechanical behaviour of crystalline molecular solids based on azobenzene dyes, which can photo-isomerize between *trans* and *cis* geometries reversibly with low-power visible light.<sup>6,9,22,45</sup> Single crystal X-ray diffraction analysis revealed that the crystal structure of (*trans*-azo)(dioxane) is based on zig-zag chains held by I $\cdots$ O halogen bonds occupying the equatorial positions of the oxygen atoms ( $d(\text{I}\cdots\text{O}) = 2.981(3)$  Å,  $R_{\text{XB}} = 0.852$ ) (Fig. 1b).<sup>46,47</sup> Single crystals of (*trans*-azo)(dioxane) exhibit strong dichroism under plane-polarized light, changing from dark red to almost completely colorless, reflecting the parallel alignment of azo-chromophores in the structure (Supplementary Fig. 6).<sup>9</sup>

Unexpectedly, irradiating the largest (010) face (Fig. 1c) of the thin, lath-shaped crystals of (*trans*-azo)(dioxane) (thickness  $\sim 5\text{--}100$  μm) using a low-power diode green laser system (Fig. 1d; 532 nm wavelength, 2–20 mW power with a beam width of  $\sim 500$  μm, see Methods, and Supplementary Information Fig. 5) resulted in cutting and the appearance of visible holes or slits at the spot of irradiation (Supplementary Figs. 7 and 8). Cutting was readily observed even for much thicker crystal samples (ca. 250 μm, Supplementary Fig. 9), at a comparable laser power (15 mW), and was not observed to depend on the face being directly cut. This laser machining behaviour contrasts with previous reports on crystalline azobenzenes which, if photoactive, exhibit either reversible or irreversible bending upon exposure to UV or visible light.<sup>6,22,32,48</sup> In order to gain further insight into the observed light-induced machining, we turned to spectroscopic observation using confocal Raman microscopy.<sup>49</sup> Due to the larger numerical aperture (reducing

the beam width 5–50  $\mu\text{m}$ ), the confocal Raman microscope setup enabled the machining of (*trans-azo*)(dioxane) crystals at even lower power levels, down to 0.5 mW, and with fine computer spatial control that permitted improved (micrometer-scale) engraving precision (Fig. 1e). By combining an optical microscope and a Raman spectrometer, this technique also allowed the real-time visualization and spectroscopic monitoring of molecular and physical changes during crystal machining, with a spatial resolution below 1  $\mu\text{m}$ , and using a laser probe with either a 532 or 785 nm wavelength. Focusing the analysis on the spectral region above 150  $\text{cm}^{-1}$ , associated with intramolecular vibrations, it was further possible to distinguish between the pure *trans-azo* and the corresponding cocrystals.

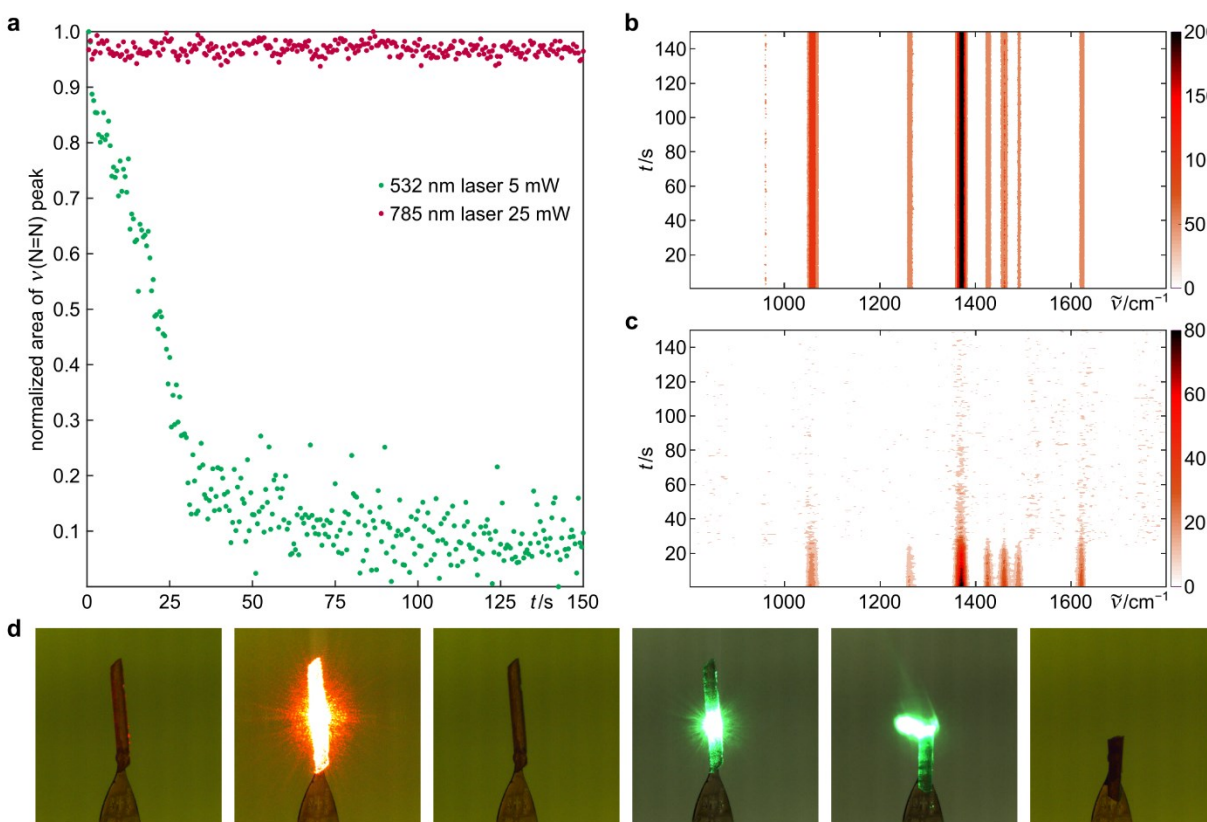


**Fig. 2 Wavelength dependence of the machining of (*trans-azo*)(dioxane) cocrystal with visible light.** **a**, Normalized area of the  $\nu(\text{N}=\text{N})$  Raman band ( $1372\text{ cm}^{-1}$ ) over time, for both 785 nm and

532 nm studies. Contour plots of Raman absorption bands over time for cocrystal (*trans-azo*)(dioxane) at different laser wavelengths and power, yet with the same beam width: **b**, 785 nm, 25 mW, **c**, 532 nm, 5 mW. **d**, Single crystal of (*trans-azo*)(dioxane) irradiated with 633 nm laser at 30 mW, followed by irradiating with 532 nm laser at 10 mW. The beam width remained constant.

Analysis by confocal Raman microscopy showed that the irradiation of (*trans-azo*)(dioxane) using near-infrared (NIR) laser light (785 nm) resulted in no visual changes to the material, even at the maximum power setting (70 mW), contrasting the machining effect observed with low-power green (532 nm) light. To confirm this observation, we collected consecutive Raman spectra for 200 seconds using either the 785 nm NIR laser at the 25 mW power setting, or the 532 nm green laser at the power setting of 5 mW (Fig. 2a and b). Irradiation at 785 nm did not lead to any noticeable changes to the spectra, whereas spectral peaks acquired using 532 nm radiation were found to diminish over time, consistent with the creation of a hole coincident with the irradiation. Specifically, the normalized intensity of the  $\nu(\text{N}=\text{N})$  Raman band was constant upon irradiation of the crystal with 785 nm light, but rapidly decayed upon exposure to 532 nm light. The band intensity plateaued after 60 seconds, with the residual signal assigned to scattering from the edges of the beam profile (Fig. 2c). No new Raman signals appeared during or after the disappearance of the  $\nu(\text{N}=\text{N})$  band, indicating the absence of new chemical species or chemical degradation. The sensitivity of (*trans-azo*)(dioxane) to irradiation at 532 nm, but not to 785 nm, is consistent with the absorption behaviour of *trans-azo*, which exhibits a  $n \rightarrow \pi^*$  transition absorption maximum centered at 460 nm (Supplementary Fig. 1). Similar experiments were visualized using the laboratory laser system (Fig. 2d), where irradiation of a single crystal with a 633 nm laser at

30 mW power resulted in no visual change to the crystal. This was followed by irradiation of the crystal by a 532 nm laser with an output power of 10 mW, resulting in clean cutting of the crystal.

The crystal machining effect was associated with loss of the volatile dioxane, as evidenced by Raman spectra obtained using the 785 nm probe before and after exposing a fresh crystal of (*trans-azo*)(dioxane) to a 1 mW 532 nm 1 second laser pulse. Spectra acquired before and after the pulse showed the disappearance of a Raman band at  $830\text{ cm}^{-1}$ , associated with the  $\nu(\text{ring breathing})$  vibration of dioxane, assigned with the help of the calculated gas-phase vibrational spectra of dioxane and *trans-azo* (Methods, Supplementary Fig., 10 Supplementary Table 2). This suggests the loss of dioxane upon irradiation (Supplementary Fig. 11). A Raman spectrum recorded from the edge of a hole previously carved with a 532 nm laser beam also revealed the absence of the band at  $830\text{ cm}^{-1}$ , again indicating dioxane loss (Supplementary Fig. 12).

Utilizing the confocal microscope-guided laser beam, a variety of more complex patterns could be gently inscribed onto single crystals of (*trans-azo*)(dioxane) (Fig. 3), either by fully penetrating through the crystal or by deep engraving of the crystal surface. Examples in Fig. 3 demonstrate the precision of such CLMS on the order of microns ( $\mu\text{m}$ ) and illustrate the variety of techniques that can be used to create (embossing and outline carving) and view (optical and fluorescence microscopy) the obtained patterns. Additionally, adjusting the power of the incident light (15, 10, 5, 2 mW) changed the diameter of the desired hole (17, 16, 14, 12  $\mu\text{m}$  respectively, Fig. 3d). The inscribed images do not exhibit any significant fading over at least 4 days (Supplementary Fig. 13).

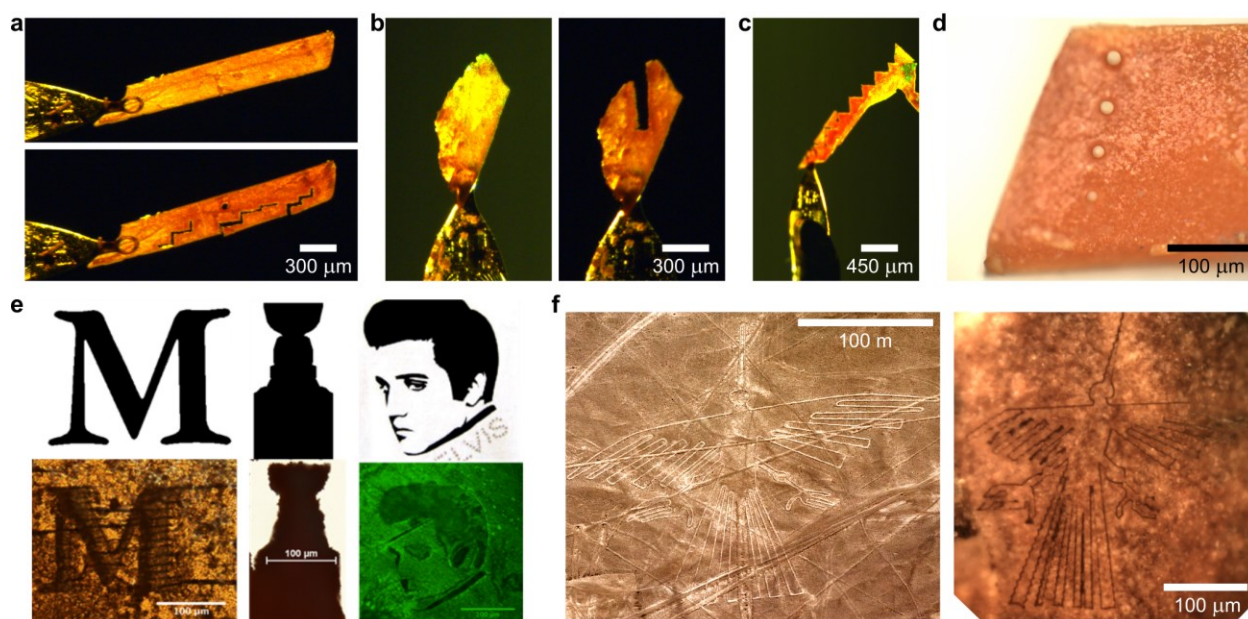


**Fig. 3 Detailed patterns inscribed onto a (*trans*-azo)(dioxane) crystal using either a laboratory laser setup (a-c), or a confocal microscope system (d-f). a**, Lines and holes inscribed into a crystal with low-power 532 nm laser. **b**, Larger slits machined into a crystal by changing the distance between the crystal and the focal point of the laser. **c**, A crystal manually machined in the shape of a staircase. **d**, A sequence of decreasingly-sized holes machined into the crystal by changing the power of the laser with a confocal microscope system (From top to bottom: 15, 10, 5, 2 mW). **e**, Top: Desired test outlines, Bottom: (left to right) Achieved outcomes of an embossed letter “M”, shown in transmission mode of an optical microscope; Microscopy image of a crystal that was cut into the iconic ‘Stanley Cup’ hockey trophy shape, by irradiating a crystal covered with a mask; Embossed image of Elvis Presley, shown under fluorescence microscopy. **f**, Another well recognized test image is the Condor of the Nazca desert (Peru, left, Credit: iStock.com/digitalg) and an analogous, approximately million-fold reduced, image imprinted onto the surface of a (*trans*-**azo**)(dioxane) crystal (right).



Single-crystal Raman spectroscopy indicated that the clean machining of thin (*trans-azo*)(dioxane) crystals is associated with dioxane loss, which was also supported by powder X-ray diffraction (PXRD) studies of the bulk microcrystalline powder of the material. PXRD analysis of a polycrystalline sample of (*trans-azo*)(dioxane) before and after 2 hours irradiation with dispersed 37 mW LED light of 532 nm wavelength revealed complete disappearance of the X-ray reflections of the cocrystal, and the appearance of signals not consistent with the reported *trans-azo* crystal structure (herein termed *trans-azo I*, Supplementary Fig. 14). Specifically, the PXRD pattern of the irradiated material changed rapidly to reveal a new crystalline phase which was subsequently identified as a polymorph of *trans-azo*, herein termed *trans-azo II*, and was obtained as diffraction-quality single crystals by rapid recrystallization from diethyl ether.

Thermogravimetric analysis coupled with differential scanning calorimetry (TGA/DSC) of (*trans-azo*)(dioxane) revealed a mass loss step taking place between 70 and 90 °C, consistent with a low temperature barrier for dioxane loss (calculated for dioxane: 13.2, measured: 14.7%). A small exothermic signal was observed in the DSC trace between 140 and 150 °C, which was attributed to the polymorphic transition *trans-azo II* → *trans-azo I*. This is followed by a larger endothermic signal at 200 °C corresponding to the melting of *trans-azo I* (Supplementary Fig. 15). The interpretation of DSC data was validated by variable-temperature PXRD analysis (Supplementary Fig. 16). A PXRD pattern collected at 25 °C was an excellent match to the one simulated for (*trans-azo*)(dioxane). Upon heating to 115 °C, the pattern showed a mixture of phases dominated by *trans-azo II* which, upon heating to 160 °C, fully converted to *trans-azo I*.

Investigation by optical hot-stage microscopy reveals that thermally induced loss of dioxane from a (*trans-azo*)(dioxane) crystal does not significantly perturb its shape

(Supplementary Fig. 17). This observation, which is consistent across several explored crystals, is likely to be critical for the high regularity of cocrystal machining.

To monitor the changes upon CLMS of (*trans*-**azo**)(dioxane) cocrystals in more detail, the laboratory laser setup was equipped with a high-speed laser beam shutter and a high-speed camera. A cocrystal was irradiated via a 532 nm laser pulses between 40 and 143 ms in length, at a constant power output of 10 mW, and with a recording rate of 1000 frames per second (fps). Crystals showed different response to light depending on the irradiation duration of the crystal. Even at short irradiation times (40 ms), the crystals were observed to emit a visibly opaque fog of outgassing (Supplementary Figs. 18–21). At longer irradiation times (143 ms), larger holes are formed, with more opaque fog emanating from the crystal. The fog was tentatively assigned to condensation of dioxane expelled from the cocrystal, and we envision its formation as being analogous of the explosive boiling phenomenon observed in high-energy machining of organic polymers.<sup>38</sup>

### **Irradiation and attempted shaping of pure *trans*-azo solid**

As a control, attempts to machine a single crystal of pure *trans*-**azo** **I** using the confocal microscopy system revealed no changes upon irradiation with the 532 nm laser at low power (<10 mW). Laser power above 15 mW, however, led to a machining effect, but accompanied by crystal cracking and/or visible displacement of material from the center towards the edge of the irradiated area (Supplementary Fig. 22a). Confocal Raman spectroscopy surface mapping revealed height differences of up to 10  $\mu\text{m}$  in the vicinity of the irradiated crystal area, but without any indication of chemical changes. The Raman signals were identical across all surface features of the irradiated crystal, with the exception of the laser-induced hole that was readily detected by the disappearance of Raman bands (Supplementary Figs. 22b and c). The mapping studies indicate that the laser-

induced displacement of the material is non-destructive, and analogous to the light-induced surface fluidization seen in azobenzene-containing polymer films.<sup>50–52</sup> These observations indicate that the ability to cleanly ‘machine’ (*trans-azo*)(dioxane) using low-power visible light is an emergent property of the cocrystal formation.

### Cocrystal laser micro-shaping of (*trans-azo*)(pyrazine)

To investigate a similar system exhibiting CLMS potential, we designed a second cocrystal based on *trans-azo* as a halogen bond donor, with pyrazine (volatile solid) as the halogen bond acceptor.<sup>53</sup> We expected the two pyridine-like nitrogen atoms of pyrazine to be much stronger XB acceptors than the ether oxygen atoms in dioxane, therefore increasing the overall stability of the resulting cocrystal. The cocrystal (*trans-azo*)(pyrazine) consists of anticipated linear chains of alternating XB donors and acceptors held *via* I⋯N interactions ( $d(\text{I} \cdots \text{N}) = 2.840(3) \text{ \AA}$ ,  $R_{\text{XB}} = 0.805$ ) (Fig. 4a). As expected from such a structure, (*trans-azo*)(pyrazine) also exhibits strong dichroism in plane-polarized light, changing the colour from dark red to light yellow depending on the orientation relative to the plane of polarization (Supplementary Fig. 23).

A single crystal of (*trans-azo*)(pyrazine) was readily machined or cut *via* low-powered light, while retaining crystallinity (Fig. 4b,c). To investigate the retention of cocrystal structure for both (*trans-azo*)(pyrazine) and (*trans-azo*)(dioxane) upon machining, a full X-ray diffraction dataset was collected for a sample of each cocrystal, after which the crystals were cut in half using a 532 nm 15 mW laser, and the full dataset recorded again for the resulting bottom half of each crystal (Fig. 4b,c, Supplementary Figs. 24 and 25). In both cases, the diffraction data collected on the daughter crystals consisted predominantly of respective cocrystal phases, demonstrating that CLMS is a localized phenomenon which does not change the extended structure of the irradiated crystal as a whole.

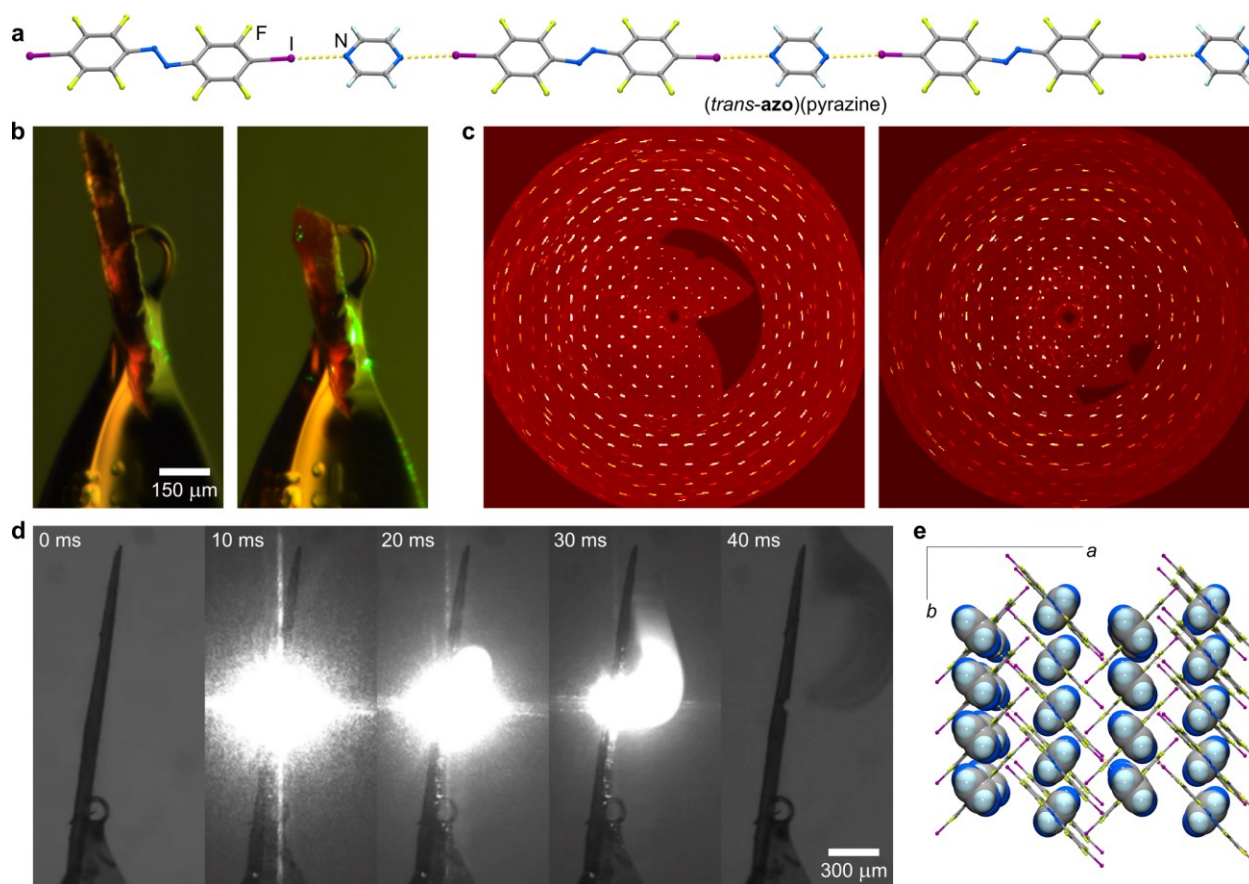


**Fig. 4. CLMS of (*trans*-azo)(pyrazine) cocrystal.** **a**, Halogen-bonded chains in the crystal structure of (*trans*-azo)(pyrazine). **b**, (*trans*-azo)(pyrazine) before (left) and after (right) cutting using a 532 nm laser (power = 15 mW). **c**, Precession image showing the 0kl layer of the cocrystal in part a, before (left) and after (right) irradiation. **d**, CLMS of (*trans*-azo)(pyrazine) cocrystal using a 40 ms pulse of the 532 nm laser light monitored by a high-speed camera. **e**, Packing of molecules in the crystal structure of (*trans*-azo)(pyrazine), viewed along the [001] direction, with *trans*-azo molecules shown in stick and pyrazine molecules in the space-filling mode.

Analogous to the (*trans*-azo)(dioxane) cocrystal, Raman microscopy was used to study the machining of the (*trans*-azo)(pyrazine) cocrystal. Based on the calculated gas-phase spectra of *trans*-azo and pyrazine, we assigned the characteristic Raman band at  $1023\text{ cm}^{-1}$  in the spectrum

of the (*trans*-**azo**)(pyrazine) cocrystal to a  $\nu$ (ring breathing) vibration of pyrazine (Supplementary Fig. 26, Supplementary Table 3). Irradiation of the cocrystal with a 532 nm laser at a power of 3 mW led to the disappearance of this characteristic band (Supplementary Fig. 27), indicating cocrystal disassembly by loss of pyrazine. Notably, the 1023  $\text{cm}^{-1}$  band was still present in the Raman spectrum recorded from the very edge of the hole created by cocrystal irradiation, indicating that the loss of pyrazine is restricted to the irradiated site and does not significantly propagate through the crystal (Supplementary Fig. 28).

Next, the photo-stability of the (*trans*-**azo**)(pyrazine) cocrystal was studied in comparison to its dioxane counterpart by monitoring the time-dependent evolution of the PXRD patterns of the respective microcrystalline powder samples upon continuous irradiation by a dispersed 532 nm LED source with a power output of 37 mW. A sample of (*trans*-**azo**)(pyrazine) revealed the transformation to *trans*-**azo II** upon prolonged irradiation (Supplementary Fig. 29), with traces of the starting (*trans*-**azo**)(pyrazine) cocrystal still present even after 18 hours of irradiation. This demonstrated the higher photo-stability of (*trans*-**azo**)(pyrazine) compared to (*trans*-**azo**)(dioxane) which started converting to *trans*-**azo II** within 10 mins of irradiation and only trace quantities of the cocrystal could be detected after 2 hours (Supplementary Fig. 13).

Thermogravimetric analysis and differential scanning calorimetry (TGA/DSC) was performed on a sample of (*trans*-**azo**)(pyrazine) (Supplementary Fig. 30). The DSC trace revealed two endothermic peaks, the first of which was coupled with a mass loss of 11.9% occurring between 80 and 135 °C. The mass loss corresponds to the loss of pyrazine in the sample (calculated for pyrazine: 12.2%) and the conversion of (*trans*-**azo**)(pyrazine) to solid *trans*-**azo II**. The second endothermic peak at 196 °C was assigned to the melting point of *trans*-**azo I**. Unlike (*trans*-**azo**)(dioxane), this system does not exhibit a clear exothermic signal corresponding to the

conversion of *trans*-**azo II** to *trans*-**azo I**. This is presumably due to the endothermic loss of the halogen bond acceptor in (*trans*-**azo**)(pyrazine) taking place at a higher temperature than in (*trans*-**azo**)(dioxane), obscuring the signal corresponding to the interconversion of *trans*-**azo** polymorphs. The interpretation of DSC data was validated by variable-temperature PXRD analysis (Supplementary Fig. 31). A PXRD pattern collected at 25 °C was an excellent match to that simulated for (*trans*-**azo**)(pyrazine). Upon heating to 125 °C, the pattern showed a mixture of phases dominated by *trans*-**azo II** which, upon heating to 180 °C, fully converted to *trans*-**azo I**. A single crystal of (*trans*-**azo**)(pyrazine) was investigated by hot-stage microscopy (Supplementary Fig. 32), revealing no major changes in crystal shape before melting.

The CLMS of (*trans*-**azo**)(pyrazine) was also investigated using a laboratory laser system equipped with a high-speed shutter and a high-speed camera (Fig. 4d). Similar to the dioxane-based system, (*trans*-**azo**)(pyrazine) showed a differential response to irradiation by different laser power (Supplementary Figs. 33–35). Irradiating a crystal of ~15 µm thickness at 5 mW for 40 ms produced no response, while irradiating with a pulse of the same length but at a power of 15 mW led to fog emission. Formation of a hole by irradiating for 40 ms required a power of 20 mW for (*trans*-**azo**)(pyrazine), which is higher than 10 mW required in the case of (*trans*-**azo**)(dioxane) under analogous conditions. This suggests that, for the same length of irradiation pulse, each cocrystal exhibits a different power threshold required for CLMS. However, CLMS can also be achieved at lower power levels simply by prolonged irradiation: hole formation in a crystal of (*trans*-**azo**)(pyrazine) of comparable thickness (~15 µm) was also achieved at a power of 15 mW by irradiating for 1 second.

## Conclusion

We presented a new technique of gentle cocrystal laser micro-shaping (CLMS): the ability to use visible (532 nm) laser light, with power as low as 0.5 mW, for micrometer-precision machining and imprinting of images onto organic molecular cocrystals. The low laser power needed for the CLMS process enables precise and automated shaping and engraving of cocrystals using a commercial confocal Raman microscopy setup, and is explained by the general cocrystal design comprising a *trans*-**azo** chromophore halogen-bonded to a volatile cocrystal former such as dioxane or pyrazine. This supramolecular design, in which the light-absorbing and volatilized components are segregated and held together by non-covalent interactions, provides an opportunity to achieve micrometer control of the machining process and avoid the use of significantly higher beam power commonly used in the conventional machining of organic polymers. The critical importance of cocrystallization for enabling CLMS is evident from the herein attempted machining of the pure *trans*-**azo** solid, which requires higher power that also causes significant surface fluidization and significant loss of machining precision. In contrast, the herein explored cocrystals based on the same *trans*-**azo** component are readily cut, machined, and embossed using low-power laser light. This proof-of-principle work presents a two-fold advance in materials science: it introduces cocrystals of a photo-reversible dye with a volatile coformer as a class of materials that can be designed to be shaped and machined with micrometer precision using low-power visible light, and introduces small-molecule organic solids as a new class of materials that can be machined, in addition to much more common polymers, ceramics and metals.

## Methods:

### Synthesis:

*Trans-azo* was synthesized in one step by treatment of 4-iodo-2,3,5,6-tetrafluoroaniline with *N*-chlorosuccinimide (NCS) and 1,8-diazabicyclo[5.4.0]undec-7-ene (DBU).<sup>54</sup> All reagents and solvents were purchased from Sigma Aldrich. Cocrystallization of (*trans-azo*)(dioxane). In a typical experiment, approx. 6 mg of *trans-azo* (0.010 mmol) were dissolved in a minimal volume of (1,4-)dioxane (ca. 2 mL). The solution was left to evaporate at room temperature, yielding long, orange, lath-shaped crystals. Cocrystallization of (*trans-azo*)(pyrazine). In a typical experiment, approx. 6 mg of *trans-azo* (0.010 mmol) and 6 mg of pyrazine (0.075 mmol) were mixed with hexanes (ca. 5 mL) with methylene chloride added dropwise until all material fully dissolved. The solution was left to evaporate at room temperature, yielding prismatic red crystals.

### Powder X-ray diffraction:

Powder X-ray diffraction experiments were performed on a Bruker D8 Advance diffractometer, using CuK $\alpha$  radiation ( $\lambda = 1.54184 \text{ \AA}$ ) source operating at 40 mA and 40 kV, equipped with a Lynxeye XE linear position-sensitive detector, in the  $2\theta$  range of 4–40° with step size of 0.019° or, alternatively, on a Bruker D2 Phaser diffractometer using nickel-filtered CuK $\alpha$  radiation ( $\lambda = 1.54184 \text{ \AA}$ ) source operating at 10 mA and 30 kV, equipped with a Lynxeye linear position-sensitive detector, in the  $2\theta$ -range of 4–40°.

### Single-crystal X-ray diffraction:

Data for (*trans-azo*)(dioxane), (*trans-azo*)(pyrazine), and *trans-azo* II were collected on a Bruker D8 Venture dual-source diffractometer equipped with a PHOTON II detector and an Oxford Cryostream 800 cooling system, using mirror-monochromated MoK $\alpha$  ( $\lambda = 0.71073 \text{ \AA}$ ) or CuK $\alpha$



radiation ( $\lambda = 1.54184 \text{ \AA}$ ) from respective microfocus sources. Data were collected in a series of  $\varphi$ - and  $\omega$ -scans. APEX3 software was used for data collection, integration, and reduction.<sup>55</sup> Numerical absorption corrections were applied using SADABS-2016/2.<sup>56</sup> Structures were solved by dual-space iterative methods using SHELXT<sup>57</sup> and refined by full-matrix least-squares on  $F^2$  using all data with SHELXL<sup>58</sup> within the OLEX2<sup>59</sup> and/or WinGX<sup>60</sup> environment.

#### UV-Vis absorbance:

Absorbance measurements were collected on an Agilent Cary 300 Bio UV-Visible spectrometer. A 55 mg/L solution of *trans*-**azo** was made up in THF, the absorbance spectrum was acquired using instrument default conditions. The spectrum of the corresponding *cis*-**azo** isomer was taken following 30 min of irradiation by a 532 nm LED (37 mW).

#### Raman spectroscopy:

Raman microscopy experiments were performed on confocal Raman Witec 300 R microscope setup using two separate probe wavelengths of 785 and 532 nm. Integration time, number of accumulations and laser power were varied depending on experiment. Simulated Raman shifts were calculated by DFT using Gaussian16,<sup>61</sup> employing the B3LYP density functional.<sup>62,63</sup> Basis set 6-311G(d,p) was used for all atoms.<sup>64</sup> The basis set for iodine<sup>65</sup> was obtained from the *Basis Set Exchange*.<sup>66</sup>

#### Thermal analysis:

Thermogravimetric analysis (TGA) and differential scanning calorimetry (DSC) measurements were performed simultaneously using a Mettler-Toledo TGA/DSC 1 Star system thermobalance. The samples were placed in alumina crucibles and measurements conducted in a stream of nitrogen ( $50 \text{ cm}^3 \text{ min}^{-1}$ ) gas, at a heating rate of  $5 \text{ }^\circ\text{C min}^{-1}$ . Data collection and analysis were performed

using the Mettler-Toledo STAR<sup>e</sup> Software 16.20 program package. Alternatively, DSC measurements were performed on a TA Instruments LTD DSC2500 at a heating rate of 1 °C min<sup>-1</sup>, under a stream of nitrogen (50 cm<sup>3</sup> min<sup>-1</sup>) gas, using a hermetically closed aluminium pan.

Hot-stage microscopy was performed using a Mettler Toledo FP90 Central Processor, equipped with a Mettler FP84 HT TA Microscopy Cell. Images were obtained on an Infinity 1 Lumenera camera attached to a Leica DM2500 optical microscope, using the Studio Capture software suite. Heating was performed from 20 to 200 °C at a rate of 20 °C min<sup>-1</sup>.

#### Detailed Machining Procedure A:

Using the confocal Raman Witec 300 R 532 nm solid-state laser with a range of power settings (0.1–20 mW), and multiple objectives (10, 20, 50, and 100× Zeiss objectives with NA = 0.25, 0.5, 0.8, and 0.9, respectively), a series of detailed drawings were engraved into the crystals using a pre-made input files with listed coordinates.

#### Detailed Machining Procedure B:

Confocal machining experiments on crystals were conducted on a Zeiss 710 Multiphoton Microscope. The images were taken with a 20× PLAN APOCHROMAT, NA = 0.8, DIC objective, and the bleaching module were performed with the aid of the Zeiss ZEN software, utilizing two-photon excitation at 750 nm provided by a direct-coupled Chameleon laser.

#### Laboratory laser system including a high-speed camera:

A Redlake MotionPro Y4 (Tallahassee, FL, USA) high-speed charge-coupled device camera was used to capture machining events at 1000 frames/s. MGL-III-532 Green DPSS Laser and Lasos lasertechnik 633nm Helium-Neon laser was coupled with a tunable neutral density filter, Melles

Griot electronic controlled shutter, and a Melles Griot convex lens with a focal length of 75 mm, aligned onto a crystal mount with a 150  $\mu\text{m}$  loop (Supplementary Fig. 5).

## Acknowledgements

We thank the Natural Sciences and Engineering Research Council (NSERC) Canada for their support through Discovery (T.F., C.J.B.) and Accelerator grants (T.F.), and Vanier Graduate (O.S.B.) and Banting Postdoctoral (F.T.) Fellowships. We thank Prof. M. Harrington of McGill Chemistry for use of the confocal Raman microscope, and S. Borchers for the graphic used in Fig. 1d. We acknowledge the use of the Cedar supercomputer, enabled by WestGrid and Compute Canada.

## Competing interests

The authors declare no competing interests.

## References:

1. Mir, N. A., Dubey, R. & Desiraju, G. R. Strategy and Methodology in the Synthesis of Multicomponent Molecular Solids: The Quest for Higher cocrystals. *Acc. Chem. Res.* **2019**, *52*, 2210–2220.
2. Aitipamula, S. et al. Polymorphs, Salts, and Cocrystals: What's in a Name? *Cryst. Growth Des.* **2012**, *12*, 2147–2152.
3. Desiraju, G. R. Crystal Engineering: From Molecule to Crystal. *J. Am. Chem. Soc.* **2013**, *135*, 9952–9967.
4. Kavanagh, O. N., Croker, D. M., Walker, G. M. & Zaworotko, M. J. Pharmaceutical cocrystals: from serendipity to design to application. *Drug Discov. Today* **2019**, *24*, 796–804.

5. MacGillivray, L. R., et al. Supramolecular Control of Reactivity in the Solid State: From Templates to Ladderanes to Metal–Organic Frameworks. *Acc. Chem. Res.* **2008**, *41*, 280–291.
6. Bushuyev, O. S., Corkery, T. C., Barrett, C. J. & Friščić, T. Photo-mechanical azobenzene cocrystals and *in situ* X-ray diffraction monitoring of their optically-induced crystal-to-crystal isomerisation. *Chem. Sci.* **2014**, *5*, 3158–3164.
7. Zaworotko, M. J. Molecules to Crystals, Crystals to Molecules...and Back Again? *Cryst. Growth Des.* **2007**, *7*, 4–9.
8. Lu, B., Fang, X. & Yan, D. Luminescent Polymorphic Co-crystals: A Promising Way to the Diversity of Molecular Assembly, Fluorescence Polarization, and Optical Waveguide. *ACS Appl. Mater. Interfaces* **2020**, *12*, 31940–31951.
9. Christopherson, J.-C., Topić, F., Barrett, C. J. & Friščić, T. Halogen-Bonded Cocrystals as Optical Materials: Next-Generation Control over Light–Matter Interactions. *Cryst. Growth Des.* **2018**, *18*, 1245–1259.
10. Liu, C.-H., Niazi, M.R. & Perepichka, D.F. Strong Enhancement of  $\pi$ -Electron Donor/Acceptor Ability by Complementary DD/AA Hydrogen Bonding. *Angew. Chem. Int. Ed.* **2019**, *58*, 17312–17321.
11. Cavallo, G. et al. The Halogen Bond. *Chem. Rev.* **2016**, *116*, 2478–2601.
12. Mukherjee, A., Tothadi, S. & Desiraju, G. R. Halogen Bonds in Crystal Engineering: Like Hydrogen Bonds yet Different. *Acc. Chem. Res.* **2014**, *47*, 2514–2524.
13. Raatikainen, K. & Rissanen, K. Breathing molecular crystals: halogen- and hydrogen-bonded porous molecular crystals with solvent induced adaptation of the nanosized channels. *Chem. Sci.* **2012**, *3*, 1235–1239.
14. Metrangolo, P. et al. Nonporous Organic Solids Capable of Dynamically Resolving Mixtures of Diiodoperfluoroalkanes. *Science* **2009**, *323*, 1461–1464.
15. Catalano, L. et al. Dynamic Characterization of Crystalline Supramolecular Rotors Assembled through Halogen Bonding. *J. Am. Chem. Soc.* **2015**, *137*, 15386–15389.
16. Szell, P. M. J., Zablony, S. & Bryce, D. L. Halogen bonding as a supramolecular dynamics catalyst. *Nat. Commun.* **2019**, *10*: 916.
17. Cavallo, G. et al. Superfluorinated Ionic Liquid Crystals Based on Supramolecular, Halogen-Bonded Anions. *Angew. Chem. Int. Ed.* **2016**, *55*, 6300–6304.
18. Sinnwell, M. A. & MacGillivray, L. R. Halogen-Bond-Templated [2+2] Photodimerization in the Solid State: Directed Synthesis and Rare Self-Inclusion of a Halogenated Product. *Angew. Chem. Int. Ed.* **2016**, *55*, 3477–3480.
19. Priimagi, A., Cavallo, G., Metrangolo, P. & Resnati, G. The Halogen Bond in the Design of Functional Supramolecular Materials: Recent Advances. *Acc. Chem. Res.* **2013**, *46*, 2686–2695.
20. Saccone, M. & Catalano, L. Halogen Bonding beyond Crystals in Materials Science. *J. Phys. Chem. B*, **2019**, *123*, 9281–9290.
21. Naumov, P., Chizhik, S., Panda, M. K., Nath, N. K. & Boldyreva, E. Mechanically Responsive Molecular Crystals. *Chem. Rev.* **2015**, *115*, 12440–12490.
22. Bushuyev, O. S., Tomberg, A., Friščić, T. & Barrett, C. J. Shaping Crystals with Light: Crystal-to-Crystal Isomerization and Photomechanical Effect in Fluorinated Azobenzenes. *J. Am. Chem. Soc.* **2013**, *135*, 12556–12559.

23. Natarajan, A. et al. The Photoarrangement of  $\alpha$ -Santonin is a Single-Crystal-to-Single-Crystal Reaction: A Long Kept Secret in Solid-State Organic Chemistry Revealed. *J. Am. Chem. Soc.* **2007**, *129*, 9846–9847.
24. Chu, Q., Swenson, D. C. & MacGillivray, L. R. A Single-Crystal-to-Single-Crystal Transformation Mediated by Argentophilic Forces Converts a Finite Metal Complex into an Infinite Coordination Network. *Angew. Chem. Int. Ed.* **2005**, *44*, 3569–3572.
25. Toh, N. L., Nagarathinam, M. & Vittal, J. J. Topochemical Photodimerization in the Coordination Polymer  $[(\text{CF}_3\text{CO}_2)(\mu\text{-O}_2\text{CCH}_3)\text{Zn}]_2(\mu\text{-bpe})_2]_n$  through Single-Crystal to Single-Crystal Transformation. *Angew. Chem. Int. Ed.* **2005**, *117*, 2277–2281.
26. Biradha, K. & Santra, R. Crystal engineering of topochemical solid state reactions. *Chem. Soc. Rev.* **2013**, *42*, 950–967.
27. Sun, A., Lauher, J. W. & Goroff, N. S. Preparation of Poly(Diiododiacetylene), an Ordered Conjugated Polymer of Carbon and Iodine. *Science* **2006**, *312*, 1030–1034.
28. Kitagawa, D. et al. Control of Photomechanical Crystal Twisting by Illumination Direction. *J. Am. Chem. Soc.* **2018**, *140*, 4208–4212.
29. Tong, F., Al-Haidar, M., Zhu, L., Al-Kaysi, R. O. & Bardeen, C. J. Photoinduced peeling of molecular crystals. *Chem. Commun.* **2019**, *55*, 3709–3712.
30. Halabi, J. M., Ahmed, E., Sofela, S. & Naumov, P. Performance of molecular crystals in conversion of light to mechanical work. *Proc. Natl. Acad. Sci. U.S.A.* **2021**, *118*, e2020604118.
31. Irie, M., Fukaminato, T., Matsuda, K. & Kobatake, S. Photochromism of Diarylethene Molecules and Crystals: Memories, Switches, and Actuators. *Chem. Rev.* **2014**, *114*, 12174–12277.
32. Halabi, J. M. et al. Spatial Photocontrol of the Optical Output from an Organic Crystal Waveguide. *J. Am. Chem. Soc.* **2019**, *141*, 14966–14970.
33. Karothu, D. P. et al. Mechanically robust amino acid crystals as fiber-optic transducers and wide bandpass filters for optical communication in the near-infrared. *Nat. Commun.* **2021**, *12*:1326.
34. Yao, Y., Zhang, L., Leydecker, T. & Samorì, P. Direct Photolithography on Molecular Crystals for High Performance Organic Optoelectronic Devices. *J. Am. Chem. Soc.* **2018**, *140*, 6984–6990.
35. Sun, J. & Litchinitser, N. M. Toward Practical, Subwavelength, Visible-Light Photolithography with Hyperlens. *ACS Nano* **2018**, *12*, 542–548.
36. Desbiolles, B. X. E., Bertsch, A. & Renaud, P. Ion beam etching redeposition for 3D multimaterial nanostructure manufacturing. *Microsyst. Nanoeng.* **2019**, *5*, 11.
37. Wang, Z. et al. Patterning Organic/Inorganic Hybrid Bragg Stacks by Integrating One-Dimensional Photonic Crystals and Macrocavities through Photolithography: Toward Tunable Colorful Patterns as Highly Selective Sensors. *ACS Appl. Mater. Interfaces* **2012**, *4*, 1397–1403.
38. Ghorai, S. et al. From co-crystals to functional thin films: photolithography using [2+2] photodimerization. *Chem. Sci.* **2013**, *4*, 4304–4308.
39. Li, W. et al. Shaping Organic Microcrystals Using Focused Ion Beam Milling. *Cryst. Growth Des.* **2020**, *20*, 1583–1589.
40. Wood, M. J. et al. Femtosecond laser micromachining of co-polymeric urethane materials. *Appl. Surf. Sci.* **2019**, *483*, 633–641.

41. Guan, L., Peng, K., Yang, Y., Qiu, X. & Wang, C. The nanofabrication of polydimethylsiloxane using a focused ion beam. *Nanotechnology* **2009**, *20*, 145301.
42. Alias, M. S., et al. Enhanced Etching, Surface Damage Recovery, and Submicron Patterning of Hybrid Perovskites using a Chemically Gas-Assisted Focused-Ion Beam for Subwavelength Grating Photonic Applications. *J. Phys. Chem. Lett.* **2016**, *7*, 137–142.
43. Bei, H., Shim, S., Miller, M. K., Pharr, G. M. & George, E. P. Effects of focused ion beam milling on the nanomechanical behavior of a molybdenum-alloy single crystal. *Appl. Phys. Lett.* **2007**, *91*, 111915.
44. Vesseur, E. J. R. et al. Surface plasmon polariton modes in a single-crystal Au nanoresonator fabricated using focused-ion-beam milling. *Appl. Phys. Lett.* **2008**, *92*, 083110.
45. Vainauskas, J., Topić, F., Bushuyev, O. S., Barrett, C. J. & Frišćić, T. Halogen bonding to the azulene  $\pi$ -system: cocrystal design of pleochroism. *Chem. Commun.* **2020**, *56*, 15145–15148.
46. Lommerse, J. P. M., Stone, A. J., Taylor, R. & Allen, F. H. The Nature and Geometry of Intermolecular Interactions between Halogens and Oxygen or Nitrogen. *J. Am. Chem. Soc.* **1996**, *118*, 3108–3116.
47. Mantina, M., Chamberlin, A. C., Valero, R., Cramer, C. J. & Truhlar, D. G. Consistent van der Waals Radii for the Whole Main Group. *J. Phys. Chem. A* **2009**, *113*, 5806–5812.
48. Bushuyev, O. S., Singleton, T. A. & Barrett, C. J. Fast, Reversible, and General Photomechanical Motion in Single Crystals of Various Azo Compounds Using Visible Light. *Adv. Mater.* **2013**, *25*, 1796–1800.
49. Salzillo, T. & Brillante, A. Commenting on the photoreactions of anthracene derivatives in the solid state. *CrystEngComm* **2019**, *21*, 3127–3136.
50. Kim, K. et al. Light-Directed Soft Mass Migration for Micro/Nanophotonics. *Adv. Opt. Mater.* **2019**, *7*, 1900074.
51. Kitamura, I., Oishi, K., Hara, M., Nagano, S. & Seki, T. Photoinitiated Marangoni flow morphing in a liquid crystalline polymer film directed by super-inkjet printing patterns. *Sci. Rep.* **2019**, *9*, 2556.
52. Cheng, Y.-C., Lu, H.-C., Lee, X., Zeng, H. & Priimagi, A. Kirigami-Based Light-Induced Shape-Morphing and Locomotion. *Adv. Mater.* **2020**, *32*, 1906233.
53. Braga, D., Grepioni, F. & Lampronti, G. I. Supramolecular metathesis: co-former exchange in co-crystals of pyrazine with (*R,R*)-, (*S,S*)-, (*R,S*)- and (*S,S/R,R*)-tartaric acid. *CrystEngComm* **2011**, *13*, 3122–3124.
54. Antoine, J. A. & Lin, Q. Synthesis of Azobenzenes Using *N*-Chlorosuccinimide and 1,8-Diazabicyclo[5.4.0]undec-7-ene (DBU). *J. Org. Chem.* **2017**, *82*, 9873–9876.
55. Bruker, APEX3, Bruker AXS Inc., Madison, Wisconsin, USA, 2012.
56. Krause, L., Herbst-Irmer, R., Sheldrick, G. M. & Stalke, D. Comparison of silver and molybdenum microfocus X-ray sources for single-crystal structure determination. *J. Appl. Cryst.* **2015**, *48*, 3–10.
57. Sheldrick, G. M. SHELXT - Integrated space-group and crystal-structure determination. *Acta Cryst.* **2015**, *A71*, 3–8.
58. Sheldrick, G. M. Crystal structure refinement with SHELXL. *Acta Cryst.* **2015**, *C71*, 3–8.
59. Dolomanov, O. V., Bourhis, L. J., Gildea, R. J., Howard, J. A. K. & Puschmann, H. OLEX2: a complete structure solution, refinement and analysis program. *J. Appl. Cryst.* **2009**, *42*, 339–341.

60. Farrugia, L. J. WinGX and ORTEP for Windows: an update. *J. Appl. Cryst.* **2012**, *45*, 849–854.
61. Frisch, M. J. et al. Gaussian 16, Revision C.01, Gaussian, Inc., Wallingford, CT, 2016.
62. Becke, A. D. Density-functional thermochemistry. III. The role of exact exchange. *J. Chem. Phys.* **1993**, *98*, 5648–5652.
63. Lee, C., Yang, W. & Parr, R. G. Development of the Colle-Salvetti correlation-energy formula into a functional of the electron density. *Phys. Rev. B*, **1998**, *37*, 785–789.
64. Ditchfield, R., Hehre, W. J. & Pople, J. A. Self-Consistent Molecular-Orbital Methods. IX. An Extended Gaussian-Type Basis for Molecular-Orbital Studies of Organic Molecules. *J. Chem. Phys.* **1971**, *54*, 724–728.
65. Glukhovtsev, M. N., Pross, A., McGrath, M. P. & Radom, L. Extension of Gaussian-2 (G2) theory to bromine- and iodine-containing molecules: Use of effective core potentials. *J. Chem. Phys.* **1995**, *103*, 1878–1885.
66. Pritchard, B. P., Altarawy, D., Didier, B., Gibson, T. D. & Windus, T. L. New Basis Set Exchange: An Open, Up-to-Date Resource for the Molecular Sciences Community. *J. Chem. Inf. Model.* **2019**, *59*, 4814–4820.